nature nanotechnology

Article

Infrared nano-imaging of Dirac magnetoexcitons in graphene

Check for updates

Michael Dapolito [1,2], Makoto Tsuneto[1], Wenjun Zheng [1], Lukas Wehmeier [1,3], Suheng Xu[2], Xinzhong Chen [1,2], Jiacheng Sun[1], Zengyi Du[1], Yinming Shao [2], Ran Jing [2], Shuai Zhang [2], Adrien Bercher[4], Yinan Dong [2], Dorri Halbertal [2], Vibhu Ravindran[1,5], Zijian Zhou[1], Mila Petrovic [1], Adrian Gozar [6,7], G. L. Carr [3], Qiang Li[1,8], Alexey B. Kuzmenko [4], Michael M. Fogler[9], D. N. Basov [2]✉, Xu Du [1]✉ & Mengkun Liu [1,3]✉

Magnetic fields can have profound effects on the motion of electrons in quantum materials. Two-dimensional electron systems subject to strong magnetic fields are expected to exhibit quantized Hall conductivity, chiral edge currents and distinctive collective modes referred to as magnetoplasmons and magnetoexcitons. Generating these propagating collective modes in charge-neutral samples and imaging them at their native nanometre length scales have thus far been experimentally elusive. Here we visualize propagating magnetoexciton polaritons at their native length scales and report their magnetic-field-tunable dispersion in near-charge-neutral graphene. Imaging these collective modes and their associated nano-electro-optical responses allows us to identify polariton-modulated optical and photo-thermal electric effects at the sample edges, which are the most pronounced near charge neutrality. Our work is enabled by innovations in cryogenic near-field optical microscopy techniques that allow for the nano-imaging of the near-field responses of two-dimensional materials under magnetic fields up to 7 T. This nano-magneto-optics approach allows us to explore and manipulate magnetopolaritons in specimens with low carrier doping via harnessing high magnetic fields.

When a magnetic field is applied to a material with free charge carriers (electrons or holes), the orbital motion of the charge carriers is affected by the formation of quantized Landau levels (LLs). This Landau quantization leads to a plethora of physical phenomena, most famously the quantized Hall effect in the d.c. transport of two-dimensional systems. In optical spectroscopy, optical transitions between LLs are observed when the field-controlled cyclotron energy $\hbar\omega_c$, where ω_c is the cyclotron frequency defined below, exceeds the LL smearing due to thermal excitation or scattering processes. The cyclotron frequency is inversely proportional to the effective cyclotron mass of the electron. As such, the largest cyclotron energy gap at a given magnetic field is apparently attained in quantum materials with a linear energy–momentum

[1]Department of Physics and Astronomy, Stony Brook University, Stony Brook, NY, USA. [2]Department of Physics, Columbia University, New York, NY, USA. [3]National Synchrotron Light Source II, Brookhaven National Laboratory, Upton, NY, USA. [4]Département de Physique de la Matière Quantique, Université de Genève, Genève 4, Switzerland. [5]Department of Physics, University of California, Berkeley, CA, USA. [6]Department of Physics, Yale University, New Haven, CT, USA. [7]Energy Sciences Institute, Yale University, West Haven, CT, USA. [8]Condensed Matter Physics and Materials Science Division, Brookhaven National Laboratory, Upton, NY, USA. [9]Department of Physics, University of California at San Diego, La Jolla, CA, USA. ✉e-mail: db3056@columbia.edu; xu.du@stonybrook.edu; mengkun.liu@stonybrook.edu
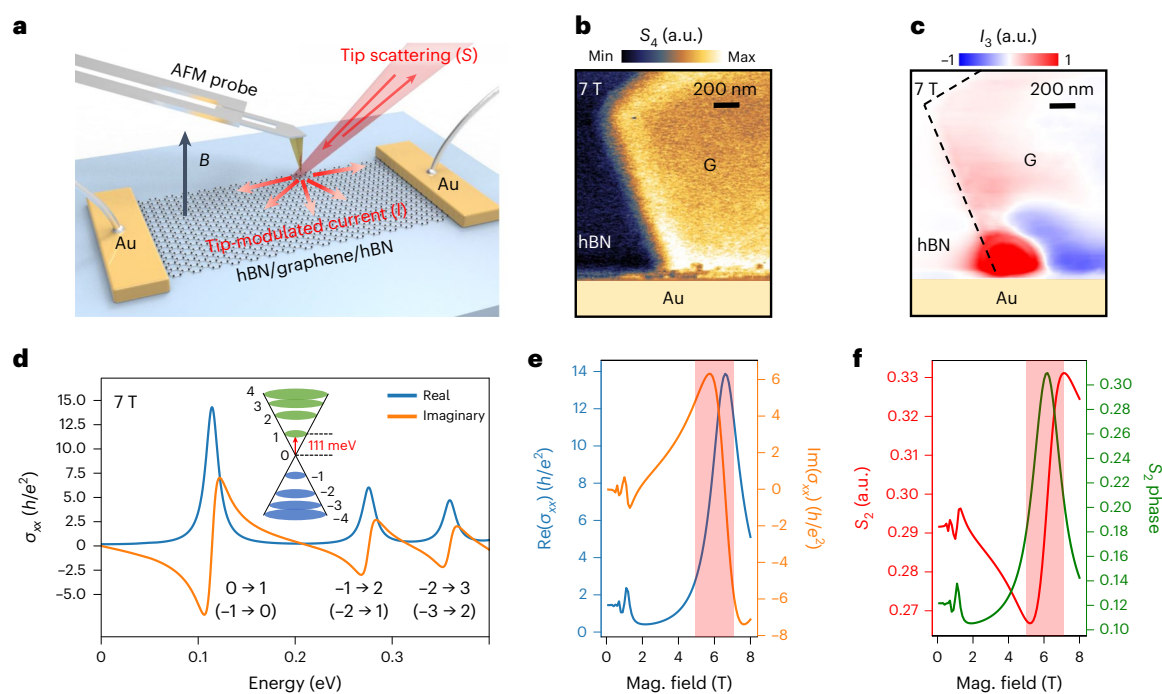
Fig. 1 | Magnetic field-dependent m-SNOM and near-field photocurrent DiME measurements of hBN-encapsulated graphene at 200 K. a, Schematic of the experimental setup. The near-field scattering amplitude (S) and photocurrent (I) can be measured simultaneously. **b**, m-SNOM image (S_4) of the hBN–graphene boundary. Graphene is labelled with G. **c**, m-SNOM near-field photocurrent images (I_3) of graphene, taken simultaneously with **b**. The graphene edge is marked with a dashed line. **d**, Calculated real (Re (σ_{xx}) ≡ σ_1, blue) and imaginary (Im (σ_{xx}) ≡ σ_2, orange) optical conductivities of graphene as functions of energy at B = 7.0 T. Parameters: Γ = 8.0 meV, v_F = 1.19 × 10^6 m s^{-1} and T = 200 K. The inset depicts the LLs superimposed on the Dirac cone of the quasiparticle dispersion in graphene. **e**,**f**, Calculated optical conductivity (**e**) and S_2 amplitude (**f**) as functions of the magnetic field at photon energy 111 meV (or 900 cm^{-1}) with the same parameter values used in **d**. The pink-shaded region indicates where the DiMEs are visible in our near-field imaging experiments. a.u. arbitrary units; mag., magnetic; max, maximum; min, minimum.

dispersion and large Fermi velocity, including graphene, as the electrons behave as massless Dirac fermions. Thus, graphene has emerged as an exemplary material for magneto-optics studies[1–5]. It exhibits the quantum Hall effect and sharp cyclotron resonances at room temperature in moderately high fields[6–8].

The applied magnetic field also alters the collective modes of electrons and holes in graphene. A unifying term for such modes is magnetoexcitons. However, their real-space features have been experimentally elusive thus far. We remark here that magnetoexcitons originating from optical transitions between adjacent LLs are also commonly referred to as magnetoplasmons[9,10]. Previous experimental work examined how plasmon eigenmodes of graphene nanostructures (for example, discs and ribbons) evolve into magnetoplasmons as the magnetic field increases. Two types of excitations have been uncovered, namely surface and edge magnetoplasmons that appear above and below the cyclotron gap, respectively[11–14]. These prior studies were carried out exclusively on doped graphene, which behaves like conventional doped semiconductors. In this work, however, we focus on graphene near the charge-neutrality point (CNP), where the charge response is qualitatively different. For example, at the CNP, the Hall conductivity σ_{xy} vanishes due to electron–hole symmetry[4,15]. To describe these modes in graphene near the CNP, we introduce the terms Dirac magnetoplasmons and Dirac magnetoexcitons (DiMEs) to emphasize the important role of the linear Dirac energy–momentum electronic dispersion near the CNP. Precisely at the CNP, 'DiME' appears to be the more appropriate term and we use it below. The DiMEs in charge-neutral graphene have been discussed theoretically[10,15,16] but have remained experimentally unexplored at infrared frequencies, as probing them with conventional diffraction-limited optics is challenging. We accomplished this task by harnessing near-field nano-infrared

techniques that involve the confinement of light to nanoscale dimensions matching the momentum and wavelength of the collective mode of interest[17,18]. Here we report a visualization of the DiMEs and a previously unreported mapping of the DiME dispersion at infrared frequencies using a home-built cryogenic magneto scanning near-field optical microscope (m-SNOM)[19]. By coupling light resonantly to the inter-LL transitions, we observed magnetic-field-tunable DiME signatures in the scattered m-SNOM signal and an accompanying photocurrent modulation at the edges of graphene.

Our technique is based on scattering-type scanning near-field optical microscopy (s-SNOM), which has made substantial progress over the last decade and led to numerous experimental achievements including polariton sensing[20–23], characterization of phase transitions[24–27] and nanoscale photocurrent detection[28–31]. m-SNOM brings forth new opportunities to explore quantum materials with broken time-reversal symmetry using nano-optics. Like traditional s-SNOM, the spatial resolution of m-SNOM is not subject to the diffraction limit of light. This is especially important at photon energies below 1 eV, where magneto-optical phenomena can now be studied on length scales as short as a few tens of nanometres. As shown below, this enables us to directly visualize the DiMEs and the associated edge-dominated d.c. photocurrent.

As in traditional s-SNOM, the key element in m-SNOM is a sharp metalized tip that concentrates incident light onto a sample, as shown schematically in Fig. 1a. The confined light interacts with the sample and is scattered back into the far field. The oscillating tip causes time-periodic oscillations of the total scattering amplitude S. The scattered signal is demodulated into its corresponding Fourier harmonics S_j of sufficiently high orders, j = 3, 4, to represent the desired near-field signals. Under common simplifying assumptions (Supplementary Note 1), one can quantitatively relate these 'demodulated' amplitudes S_j to
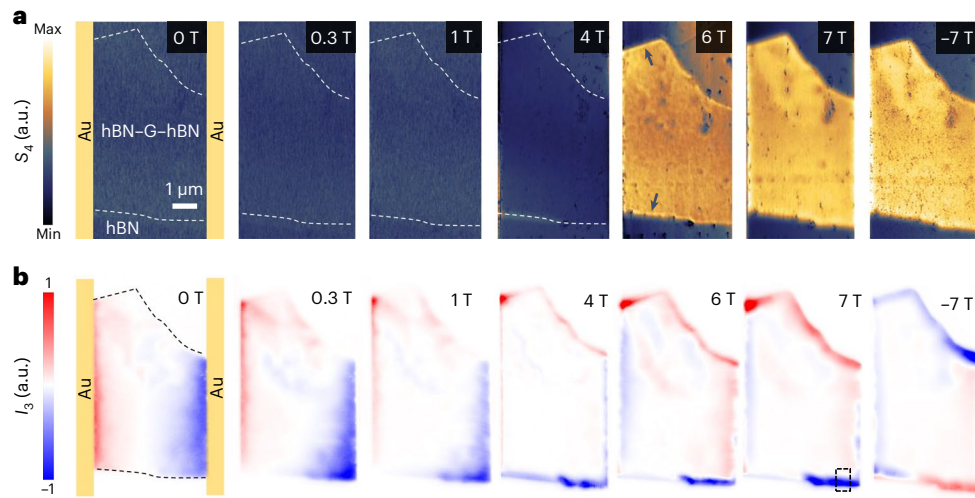
Fig. 2 | Nano-infrared images of near-charge-neutral graphene in the regime of the field-tuned 0 → 1 LL transition. a, m-SNOM images. **b**, Near-field photocurrent images. The incident light has a wavelength of ~11.2 μm (~111 meV or ~900 cm⁻¹) and the sample was kept at 200 K. The box in the bottom right corner of the sample at 7 T (**b**) shows the region we image in Figs. 3 and 4. The white dashed lines in **a** outline the boundaries of the graphene.

the optical reflection coefficient $r_p = r_p(q, \omega)$ of the sample, which is a function of the incident photon frequency ω and in-plane momentum q. In general, a larger r_p produces a larger S_j. The s-SNOM signal is strongly enhanced when ω is resonant with collective modes of the system, which give rise to the poles of $r_p(q, \omega)$. Additionally, the collective modes produce spatially periodic interference fringes along the sample edges in the s-SNOM images, as discussed below.

Resonant excitation of Dirac magnetoexcitons

To study DiMEs in real space, we use monolayer graphene encapsulated between two thin crystals of hexagonal boron nitride (hBN) with thicknesses of 5 nm (top) and 28 nm (bottom). The data presented below were taken at temperature $T = 200$ K, although similar phenomena have been observed in a wider range of temperatures from 70 to 300 K. Using electrodes fabricated on the two side edges of an hBN–graphene–hBN heterostructure, we performed scanning near-field photocurrent microscopy simultaneously with the m-SNOM measurement[29]. Representative images of these measurements are shown in Fig. 1b (S_4) and Fig. 1c (I_3, the photocurrent demodulated at the $j = 3$ harmonic of the tip tapping frequency).

Electrons in graphene near the CNP are treated as Dirac fermions with LL energies that scale as $E_{CNP} + \text{sgn}(n)\sqrt{|n|} \hbar\omega_c$, where n is the LL index, E_{CNP} is the Fermi energy at the CNP and $\hbar$ is the reduced Planck constant. Here, $\hbar\omega_c = \sqrt{2}\hbar v_F/l_B$ is the gap between the $n = 0$ and $n = 1$ LLs, where $l_B = \sqrt{\hbar/e\,|\mathbf{B}|}$ is the magnetic length, v_F is the graphene Fermi velocity and $\mathbf{B}$ is the magnetic field. At the CNP, all $n < 0$ LLs are filled, all $n > 0$ LLs are empty and the $n = 0$ level is half filled. The allowed inter-LL optical transitions are $-|n| \to |n| + 1$ and $-|n| - 1 \to |n|$, yielding resonances of the complex optical conductivity $\sigma_{xx}(\omega) = \sigma_1 + i\sigma_2$ at energies $\Delta E = \hbar\omega = \left(\sqrt{|n|} + \sqrt{|n| + 1}\right)\hbar\omega_e$ The calculated real and imaginary conductivities as a function of the photon energy are plotted in Fig. 1d. Here we assume a phenomenological momentum dissipation rate of $\Gamma = 8.0$ meV. This dissipation rate was chosen to best match the experimental magnetic-field-dependent near-field contrast and DiME dispersion of Figs. 2 and 4a, respectively. In principle, Γ will vary for different LL transitions[32]. However, since here we report only the 0 → 1 transition, we kept the dissipation rate constant for these calculations. At 7 T, the energy of the incident light in our experiment, 111 meV, is close to the principal cyclotron resonance of a bare graphene sample at $\hbar\omega_c \approx 114$ meV. In Fig. 1e, where σ_{xx} is plotted versus B, weaker resonances due to higher-n transitions at fields $B \simeq 1$ T may also be

discerned. Many-body effects, which were neglected in these calculations, cause B-dependent corrections to v_F (and, therefore, ω_c) that scale with the dimensionless coupling parameter $g = e^2/\hbar\kappa v_F \approx 1$ (refs. 33–35). Here $\kappa = \kappa_1 + i\kappa_2$ is the effective dielectric permittivity of the graphene surroundings. To account for these sample-dependent corrections, we treat v_F as an adjustable parameter. Shown in Fig. 1f, the m-SNOM signal S_2 is computed using a lightning rod model (Supplementary Note 1) with σ_{xx} as an input. The results shown in Fig. 1e,f indicate that the B-field dependence of the near-field signal faithfully reproduces the field-tunable effects rooted in cyclotron resonance physics and the attendant collective modes.

The collective mode dispersions of graphene can be derived from the magnetic-field-dependent σ_{xx}, which determines the near-field reflection coefficient $r_p(q, \omega)$ of the system. As we are measuring near-charge-neutral graphene, the off-diagonal conductivity components are omitted in our calculation. The mode dispersions are defined by the poles of $r_p(q, \omega)$ at complex $q = q_1 + iq_2$, which are distinct from highly doped graphene. The mode wavelength is $\lambda = 2\pi/q_1$ and an analytical approximation for λ of the DiMEs associated with the 0 → 1 LL transition is[15]

$$\lambda(\omega) \simeq \frac{g(\omega)}{2\pi} \frac{v_F}{(\omega - \omega_c)}, \tag{1}$$

where g is the frequency-dependent coupling parameter defined above. This equation, valid for $\lambda \gg l_B$ and $\omega \to \omega_c$, implies that the group velocity of the DiMEs is $\lesssim v_F$. In contrast, the group velocity of plasmons in doped graphene at $B = 0$ is typically much higher than v_F. Equation (1) also suggests that measuring the DiME wavelength $\lambda(\omega)$ directly probes the Fermi velocity v_F. This is in stark contrast with the plasmon polaritons in highly doped graphene, whose wavelength depends on the carrier density. The mode damping is characterized by the quality factor $Q = q_1/q_2 \approx (\sigma_1/\sigma_2 + \kappa_2/\kappa_1)^{-1}$ (refs. 11,12). Assuming that σ_1/σ_2 is the dominant quantity in this expression, Fig. 1d,e indicates that $Q > 1$ starting from frequencies exceeding ω_c by an amount ~Γ. This is the lower bound for the range of ω where propagating DiMEs exist. The term κ_2/κ_1 plays an important role when either σ_1 or σ_2 is close to zero. A theoretical upper bound of ω where DiMEs are observable with m-SNOM is set by the condition $\lambda \simeq a$. Here $a \simeq 15$ nm is the radius of curvature of the tip, which defines the spatial resolution of m-SNOM. In comparison, $l_B \approx 10$ nm at $B = 6$ T.
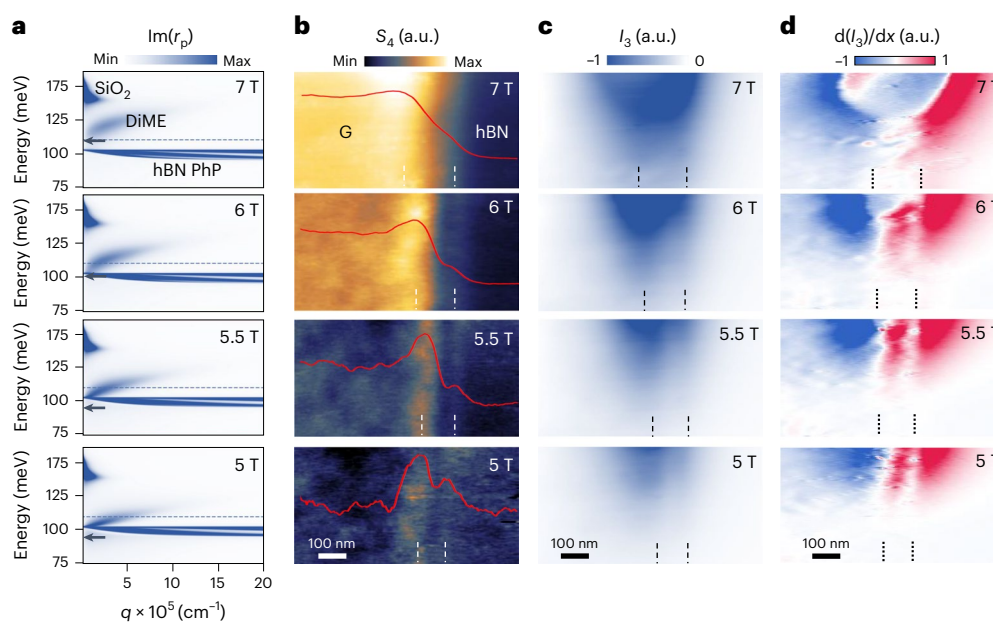
Fig. 3 | Magnetic field tuning of DiMEs. a, Calculated imaginary part of the reflection coefficient r_p illustrating the field-dependent dispersion of the collective modes in the system. The dashed lines denote our incident light frequency of ~900 cm⁻¹. The broadened curve intersecting the dashed lines is the DiME dispersion. The black arrows indicate the principal cyclotron resonances (0 → 1 LL transition) at each magnetic field. Parameters: Γ = 8.0 meV, $v_F = 1.19 \times 10^6$ m s⁻¹ and T = 200 K. **b,c**, Field-dependent m-SNOM image (**b**) and near-field photocurrent image (**c**) at the graphene–hBN boundary. The red curves in **b** are the averaged line profiles of the near-field signal (S_4). **d**, Derivative of the photocurrent signal in **c** highlighting the modulation of the edge photocurrent by the DiME. The region where the data was taken is marked by the black rectangle in Fig. 2b (note the scan area is rotated by 90° here). The dotted and dashed lines in **b**, **c** and **d** label the observed interference fringes as guides for the eyes. PhP, phonon polariton.

These unique collective modes of graphene can be directly imaged as a function of the magnetic field B, as shown in the m-SNOM images (S_4) of Fig. 2a. For $B \leq 4$ T, there is little contrast between hBN and graphene, indicating that the coupling of light to the electronic system of graphene is weak. At 6 T, the contrast between hBN and graphene becomes clearly visible and the real-space signature of propagating plasmons, namely an interference fringe, along the edge of graphene (the black arrows in the 6 T panel; also see Fig. 3b) becomes evident. At our largest field of $B = \pm 7$ T, the S_4 signal is strongly enhanced over the entire graphene sheet. Since hBN is an insulator and inert to a magnetic field, the observed evolution of the contrast must be attributed to graphene. Indeed, the observed changes in S_4 can be explained by an increased scattering of light due to the 0 → 1 LL transitions in graphene. As the B field grows, first the high-frequency tail and then the central part of this resonance become accessible at the frequency of our incident light. This interpretation is corroborated by the calculations reported in Supplementary Note 1.

Another perspective of the DiME signatures can be obtained using complementary information on the magneto-optical effects provided by imaging a nano-photocurrent with the same m-SNOM instrument. The tip-induced part of the photocurrent is captured by the third-order demodulated photocurrent signal I_3 (Fig. 2b). As asymmetry is required for local net photocurrent generation, the detected I_3 is almost negligible away from the gold electrical contacts (labelled by 'Au' in Fig. 2b) and graphene edges (dashed lines in Fig. 2b), where the graphene is largely homogeneous and, thus, possesses inversion symmetry. At the contacted and contact-free edges, the inversion symmetry is broken, leading to a finite photocurrent[29]. The photocurrent traces I_3 display a strong dependence on the field. Without the magnetic field, I_3 is uniform along the contacts. As the magnetic field increases until 4 T, shrinking photocurrent 'hot spots' at the opposite corners of the sample appear (top left and bottom right in Fig. 2b). Assuming that the photocurrent is due to the photo-thermoelectric effect[29,36] and invoking the Shockley–Ramo formalism[37–39], we surmise that these hot spots mark the locations where an enhanced current density would exist in a d.c. transport experiment. Current crowding at the corners of the sample is known to occur when the d.c. Hall conductivity σ_{xy} becomes comparable to or exceeds the diagonal d.c. conductivity σ_{xx} (Supplementary Note 3). Such a finite σ_{xy} can arise in our sample due to the residual doping of graphene.

At higher fields ($B \geq 6$ T), we observed a strong photocurrent extending along the contact-free edges of graphene. This photocurrent reverses its sign when the magnetic field is flipped from +B to −B. We attribute this edge photocurrent to a DiME-enhanced photo-Nernst effect[40,41], as detailed in Supplementary Note 3. The DiME enhancement of the photocurrent was confirmed by applying inter-LL resonant and non-resonant light and comparing the resulting photocurrent signals. For the non-resonant light (wavelength 6.59 μm and photon energy 188 meV), the photocurrent was reduced by more than an order of magnitude compared to what is seen in Fig. 2b.

Visualizing and mapping the DiME dispersion

The images in Fig. 2 contain rich insights into how magnetic-field-induced collective modes alter the real-space optical and optoelectronic properties of charge-neutral graphene. By zooming in on the graphene boundary, we can analyse the behaviour of the excitonic fringes and study the dispersion of the collective modes. Theoretically, one can visualize the collective mode dispersion by plotting the numerically computed Im(r_p) as a function of real q and ω. From such a plot (Fig. 3a), we find three classes of modes in our system: (1) waveguide phonon polaritons of hBN encapsulating layers at 92 meV < $\hbar\omega$ < 103 meV, (2) the surface phonons of the SiO₂ substrate at $\hbar\omega$ = 146 meV and (3) the DiMEs of graphene residing between (1) and (2). The DiME dispersion curve exhibits flattening and/or avoided crossings with the other modes. This behaviour originates from a decrease of parameter $g(\omega) \propto \kappa^{-1}(\omega)$ near the phonon resonances where the effective permittivity $\kappa(\omega)$ diverges. The momentum q where the DiME dispersion intersects our laser frequency (blue dashed line in Fig. 3a) decreases
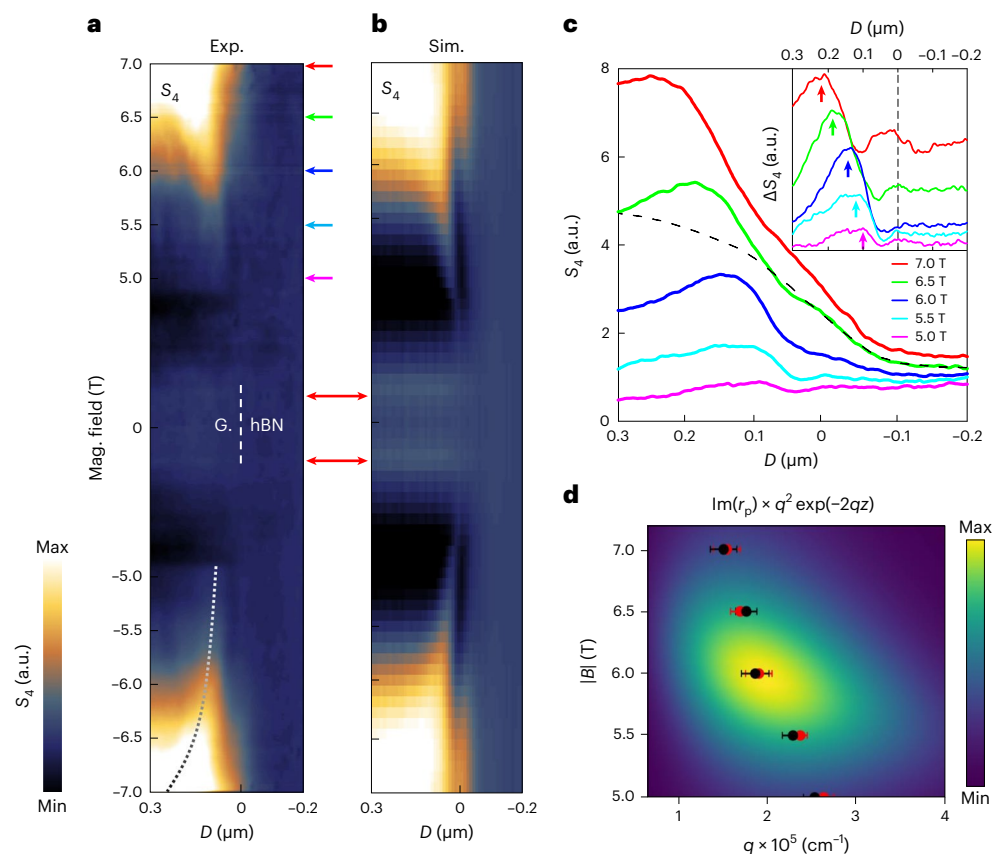
Fig. 4 | Magnetic field-dependent DiMEs dispersion. a,b, Measured (**a**) and simulated (**b**) m-SNOM line scans at the graphene–hBN boundary while sweeping the magnetic field from 7 T to −7 T. The line scans clearly show that the DiME appears between ±5 and ±7 T and disappears for magnetic fields between 0 and ±5 T. Note that the sweep of the magnetic field is reduced in speed between ±5 and ±7 T. The simulation uses the same parameter values as in Fig. 3. The double-headed red arrows indicate the faint signature of the −1 → 2 (−2 → 1) transition. The dashed curve in **a** is a guide for the eye. **c,** Line cuts from **a** showing the change in DiME wavelength from 7 to 5 T. The black dashed line shows one example of the integrated Lorentz-shaped background subtracted from the line

profile of the s-SNOM signal measured at 6.5 T. The inset shows the extracted oscillatory part of the signal, from which we extract the spacing d between fringes. **d,** Colour map showing the magnetic-field-dependent $\mathrm{Im}(r_p)$ multiplied by the tip model response function $q^2 \exp(-2qz)$, where $z \approx 50$ nm is the average tip-sample distance[56]. Black and red dots are the measured DiME wavevector $q = 2\pi/\lambda = 2\pi/2d$ at positive and negative fields, respectively. Data points are presented as the optimal wavevector plus or minus the standard deviation determined from the fitting of the peak positions in the inset of **c**. Exp., experimental; G., graphene; Mag., magnetic; Sim., simulated.

as the magnetic field increases, yielding a correspondingly larger λ at higher fields.

As shown in Fig. 3b, the fringes, spaced by $d = \lambda/2$, are caused by interference of tip-launched DiME polariton waves with their reflections off the sample boundaries[42]. The fringes become evident at magnetic fields $B \gtrsim 5$ T with the spacing increasing from ~100 nm at ±5 T to ~200 nm at ±7 T, in agreement with the rough estimates of λ we extracted from the DiME dispersion curve in Fig. 3a. Fringe-like features are also present in the photocurrent images (Fig. 3c,d). This is because oscillations of the DiME electric field intensity modulate the local thermal energy dissipation, which in turn leads to oscillations in the near-field photo-thermal electric current[43]. In general, we found that the photocurrent signal extends into the interior of the sample over a slightly longer length scale compared to the DiME fringes. This length scale, referred to as the cooling length, is determined by the interplay of the thermal conductivity of graphene and the thermal resistance of the graphene–hBN interface[22]. Note that in addition to the tip, the collective modes in graphene can be launched by any sharp boundaries or metallic structures, for example, electrical contacts. This gives rise to λ-periodic rather than $\lambda/2$-periodic fringes. At the top of the images in Fig. 3b–d there is an Au contact oriented horizontally (right side of the box in Fig. 2b (7 T)). Although the photocurrent is enhanced near this contact, we do not observe contact-launched fringes there. This is

possibly due to the contact-doping effect causing graphene to become doped away from charge neutrality in the vicinity of the electrodes[44].

To quantify the field-dependent DiME dispersion, we took line scans across the graphene–hBN boundary while sweeping the magnetic field from 7 to −7 T. As shown in Fig. 4a, the onset of the fringes occurs at around ±5 T. The curvature of the interference fringes (dashed trace in Fig. 4a) suggests that there are longer wavelengths (lower q) at higher fields. We used a commercial finite-element solver to simulate the DiME interference fringes with the same parameter values as in Fig. 3a[45]. The simulation results, depicted in Fig. 4b, qualitatively agree with our experimental observations in Fig. 4a. This provides clear evidence that the observed changes in the edge fringes originate from the field-dependent DiME dispersion. Note that a slight brightening of the s-SNOM signal at around 1.1 T can also be seen in Fig. 4a,b (double-headed red arrows). We attribute this to the weaker −1 → 2 (−2 → 1) LL transition (Fig. 1d). With an improved signal-to-noise ratio, future experiments can explore this and other higher order LL transitions. In addition, potential modifications to the DiME dispersion due to the bending of the LLs caused by quantum Hall edge states can also be examined, preferably at lower temperatures.

Shown in Fig. 4c are line cuts of the s-SNOM signal taken along the horizontals corresponding to the coloured arrows in Fig. 4a. These are used to determine λ quantitatively. By fitting the derivative of these

line cuts to an asymmetric Lorentz function[46], the background can be subtracted to reveal readily apparent fringes, as shown in the inset of Fig. 4c. The estimates of λ obtained from this fitting were converted to the wavevector $q = 2\pi/\lambda$ and are shown as dots in Fig. 4d. The DiME wavelength increases monotonically from ~240 nm at 5 T to ~400 nm at 7 T, in good agreement with the theoretical predictions represented by the colour map in Fig. 4d.

Conclusions

The propagation of DiMEs results in the formation of standing wave fringes and modulated photocurrent pathways at the sample edges. These can be observed only by using sub-diffractional imaging systems coupled to high magnetic fields. The DiME dispersion is extremely responsive to magnetic fields as it originates from inter-LL transitions. Consequently, the collective mode energies are expected to be adjustable across a wide frequency range from microwave and terahertz (millielectronvolts) to infrared and visible (electronvolts), providing an extensive scope for exploration in future research using m-SNOM. Given that the DiME exists at charge neutrality, it can be used to study many-body effects rooted in electron–electron interactions or hydrodynamic physics under the influence of a magnetic field[47]. Chiral polaritons[48], proximity effects[49] or possibly strong mode coupling[50] can be investigated with DiME-based systems. Additionally, the frequency-dependent absorption edge of the DiMEs is highly sensitive to the LL filling and scattering rate. This can be useful for studying the flat band physics in graphene and other low-dimensional systems (for example, moiré modulated v_F) subject to magnetic fields[51,52]. Thus, the m-SNOM technique developed for this work is the first step toward the study of the magneto-optical properties of quantum materials at the nanoscale. In combination with terahertz near-field microscopy or terahertz near-field emission spectroscopy, m-SNOM can also be performed with various types of Dirac and Weyl semimetals[23,30], in which a magnetic field is predicted to induce chiral anomalies, along with other intriguing phenomena such as non-reciprocal polaritons, multi-photonic bands, and frequency and polarization conversion[11,12,53–55].

Online content

Any methods, additional references, Nature Portfolio reporting summaries, source data, extended data, supplementary information, acknowledgements, peer review information; details of author contributions and competing interests; and statements of data and code availability are available at https://doi.org/10.1038/s41565-023-01488-y.

References

1. Peres, N. M. R., Guinea, F. & Castro Neto, A. H. Electronic properties of disordered two-dimensional carbon. *Phys. Rev. B Condens. Matter Mater. Phys.* **73**, 125411 (2006).
2. Sadowski, M. L., Martinez, G., Potemski, M., Berger, C. & De Heer, W. A. Landau level spectroscopy of ultrathin graphite layers. *Phys. Rev. Lett.* **97**, 266405 (2006).
3. Jiang, Z. et al. Infrared spectroscopy of Landau levels of graphene. *Phys. Rev. Lett.* **98**, 197403 (2007).
4. Gusynin, V. P., Sharapov, S. G. & Carbotte, J. P. Magneto-optical conductivity in graphene. *J. Phys. Condens. Matter* **19**, 026222 (2007).
5. Crassee, I. et al. Giant Faraday rotation in single- and multilayer graphene. *Nat. Phys.* **7**, 48–51 (2011).
6. Crassee, I. et al. Multicomponent magneto-optical conductivity of multilayer graphene on SiC. *Phys. Rev. B Condens. Matter Mater. Phys.* **84**, 035103 (2011).
7. Goerbig, M. O. Electronic properties of graphene in a strong magnetic field. *Rev. Mod. Phys.* **83**, 1193 (2011).
8. Orlita, M. et al. Approaching the Dirac point in high-mobility multilayer epitaxial graphene. *Phys. Rev. Lett.* **101**, 267601 (2008).
9. Kallin, C. & Halperin, B. I. Excitations from a filled Landau level in the two-dimensional electron gas. *Phys. Rev. B* **30**, 5655 (1984).
10. Lozovik, Y. E. & Sokolik, A. A. Influence of Landau level mixing on the properties of elementary excitations in graphene in strong magnetic field. *Nanoscale Res. Lett.* **7**, 134 (2012).
11. Wang, W., Apell, S. P. & Kinaret, J. M. Edge magnetoplasmons and the optical excitations in graphene disks. *Phys. Rev. B Condens. Matter Mater. Phys.* **86**, 125450 (2012).
12. Andreev, I. V., Muravev, V. M., Semenov, N. D., Zabolotnykh, A. A. & Kukushkin, I. V. Magnetodispersion of two-dimensional plasmon polaritons. *Phys. Rev. B* **104**, 195436 (2021).
13. Petković, I., Williams, F. I. B. & Glattli, D. C. Edge magnetoplasmons in graphene. *J. Phys. D: Appl. Phys.* **47**, 094010 (2014).
14. Poumirol, J. M. et al. Electrically controlled terahertz magneto-optical phenomena in continuous and patterned graphene. *Nat. Commun.* **8**, 14626 (2017).
15. Slipchenko, T. M., Poumirol, J. M., Kuzmenko, A. B., Nikitin, A. Y. & Martín-Moreno, L. Interband plasmon polaritons in magnetized charge-neutral graphene. *Commun. Phys.* **4**, 110 (2021).
16. Iyengar, A., Wang, J., Fertig, H. A. & Brey, L. Excitations from filled Landau levels in graphene. *Phys. Rev. B Condens. Matter Mater. Phys.* **75**, 125430 (2007).
17. Keilmann, F. & Hillenbrand, R. Near-field microscopy by elastic light scattering from a tip. *Phil. Trans. R. Soc. A* **362**, 787–805 (2004).
18. Chen, X. et al. Modern scattering-type scanning near-field optical microscopy for advanced material research. *Adv. Mater.* **31**, 1804774 (2019).
19. Dapolito, M. et al. Scattering-type scanning near-field optical microscopy with Akiyama piezo-probes. *Appl. Phys. Lett.* **120**, 013104 (2022).
20. Fei, Z. et al. Edge and surface plasmons in graphene nanoribbons. *Nano Lett.* **15**, 8271–8276 (2015).
21. Sunku, S. S. et al. Photonic crystals for nano-light in moiré graphene superlattices. *Science* **362**, 1153–1156 (2018).
22. Lundeberg, M. B. et al. Thermoelectric detection and imaging of propagating graphene plasmons. *Nat. Mater.* **16**, 204–207 (2017).
23. Jing, R. et al. Terahertz response of monolayer and few-layer WTe₂ at the nanoscale. *Nat. Commun.* **12**, 5594 (2021).
24. Qazilbash, M. M. et al. Mott transition in VO₂ revealed by infrared spectroscopy and nano-imaging. *Science* **318**, 1750–1753 (2007).
25. McLeod, A. S. et al. Nanotextured phase coexistence in the correlated insulator V₂O₃. *Nat. Phys.* **13**, 80–86 (2017).
26. Post, K. W. et al. Coexisting first- and second-order electronic phase transitions in a correlated oxide. *Nat. Phys.* **14**, 1056–1061 (2018).
27. Stinson, H. T. et al. Imaging the nanoscale phase separation in vanadium dioxide thin films at terahertz frequencies. *Nat. Commun.* **9**, 3604 (2018).
28. Sunku, S. S. et al. Nano-photocurrent mapping of local electronic structure in twisted bilayer graphene. *Nano Lett.* **20**, 2958–2964 (2020).
29. Woessner, A. et al. Near-field photocurrent nanoscopy on bare and encapsulated graphene. *Nat. Commun.* **7**, 10783 (2016).
30. Shao, Y. et al. Nonlinear nanoelectrodynamics of a Weyl metal. *Proc. Natl Acad. Sci. USA* **118**, e2116366118 (2021).
31. Sunku, S. S. et al. Hyperbolic enhancement of photocurrent patterns in minimally twisted bilayer graphene. *Nat. Commun.* **12**, 1641 (2021).
32. Nedoliuk, I. O., Hu, S., Geim, A. K. & Kuzmenko, A. B. Colossal infrared and terahertz magneto-optical activity in a two-dimensional Dirac material. *Nat. Nanotechnol.* **14**, 756–761 (2019).
33. Kotov, V. N., Uchoa, B., Pereira, V. M., Guinea, F. & Castri Neto, A. H. Electron-electron interactions in graphene: current status and perspectives. *Rev. Mod. Phys.* **84**, 1067 (2012).

34. Shizuya, K. Many-body corrections to cyclotron resonance in monolayer and bilayer graphene. *Phys. Rev. B* **81**, 075407 (2010).

35. Henriksen, E. A. et al. Interaction-induced shift of the cyclotron resonance of graphene using infrared spectroscopy. *Phys. Rev. Lett.* **104**, 067404 (2010).

36. Xu, X., Gabor, N. M., Alden, J. S., Van Der Zande, A. M. & McEuen, P. L. Photo-thermoelectric effect at a graphene interface junction. *Nano Lett.* **10**, 562–566 (2010).

37. Checkelsky, J. G. & Ong, N. P. Thermopower and Nernst effect in graphene in a magnetic field. *Phys. Rev. B* **80**, 081413(R) (2009).

38. Wei, P., Bao, W., Pu, Y., Lau, C. N. & Shi, J. Anomalous thermoelectric transport of Dirac particles in graphene. *Phys. Rev. Lett.* **102**, 166808 (2009).

39. Lundeberg, M. B. & Koppens, F. H. L. Thermodynamic reciprocity in scanning photocurrent maps. Preprint at https://arxiv.org/abs/2011.04311 (2020).

40. Cao, H. et al. Photo-Nernst current in graphene. *Nat. Phys.* **12**, 236–239 (2016).

41. Olbrich, P. et al. Giant photocurrents in a Dirac fermion system at cyclotron resonance. *Phys. Rev. B Condens. Matter Mater. Phys.* **87**, 235439 (2013).

42. Fei, Z. et al. Gate-tuning of graphene plasmons revealed by infrared nano-imaging. *Nature* **486**, 82–85 (2012).

43. Alonso-González, P. et al. Acoustic terahertz graphene plasmons revealed by photocurrent nanoscopy. *Nat. Nanotechnol.* **12**, 31–35 (2016).

44. Giubileo, F. & Di Bartolomeo, A. The role of contact resistance in graphene field-effect devices. *Prog. Surf. Sci.* **92**, 143–175 (2017).

45. Chen, X. et al. Rapid simulations of hyperspectral near-field images of three-dimensional heterogeneous surfaces—part II. *Opt. Express* **30**, 11228 (2022).

46. Maissen, C., Chen, S., Nikulina, E., Govyadinov, A. & Hillenbrand, R. Probes for ultrasensitive THz nanoscopy. *ACS Photonics* **6**, 1279–1288 (2019).

47. Xin, N. et al. Giant magnetoresistance of Dirac plasma in high-mobility graphene. *Nature* **616**, 270–274 (2023).

48. Li, Q. et al. Chiral magnetic effect in $ZrTe_5$. *Nat. Phys.* **12**, 550–554 (2016).

49. Tseng, C. C. et al. Gate-tunable proximity effects in graphene on layered magnetic insulators. *Nano Lett.* **22**, 8495–8501 (2022).

50. Bloch, J., Cavalleri, A., Galitski, V., Hafezi, M. & Rubio, A. Strongly correlated electron–photon systems. *Nature* **606**, 41–48 (2022).

51. Ma, C. et al. Moiré band topology in twisted bilayer graphene. *Nano Lett.* **20**, 6076–6083 (2020).

52. Yu, J. et al. Correlated Hofstadter spectrum and flavour phase diagram in magic-angle twisted bilayer graphene. *Nat. Phys.* **18**, 825–831 (2022).

53. Hu, B., Tao, J., Zhang, Y. & Wang, Q. J. Magneto-plasmonics in graphene-dielectric sandwich. *Opt. Express* **22**, 21727 (2014).

54. Yan, H. et al. Infrared spectroscopy of tunable Dirac terahertz magneto-plasmons in graphene. *Nano Lett.* **12**, 3766–3771 (2012).

55. Kim, R. H. J., Park, J.-M., Haeuser, S. J., Luo, L. & Wang, J. A sub-2 Kelvin cryogenic magneto-terahertz scattering-type scanning near-field optical microscope (cm-THz-sSNOM). *Rev. Sci. Instrum.* **94**, 043702 (2023).

56. Fei, Z. et al. Infrared nanoscopy of Dirac plasmons at the graphene-SiO_2 interface. *Nano Lett.* **11**, 4701–4705 (2011).

Methods

Closed-cycle m-SNOM

Infrared nano-imaging capabilities at cryogenic temperatures and under magnetic fields up to 7 T were demonstrated using a closed-cycle cryostat (Opticool, Quantum Design) in Mengkun Liu's lab at Stony Brook University. The scanning stages and positioners were from Attocube (ANSxyz100/LT/UHV and ANPxyz101/LT/UHV, respectively). The mechanical noise in s-SNOM was less than 0.5 nm in the z direction and less than 20 nm in the xy direction (resolution limited) at 100 K. Our atomic force microscope (AFM) has a spatial resolution of about 15 nm and a scan area of 50×50 µm^2 at room temperature. The accessible temperature range of our home-built scanning probe system is ~10–350 K. A CO_2 laser centred at ~11 um and a quantum cascade laser centred at 6.4 µm, both operating in continuous wave operation at room temperature, were used for the photocurrent and s-SNOM imaging. The laser power before entering the cryostat was around 12 mW and was reduced to below 10 mW at the tip due to reflections from the cryostat window. The laser was focused onto the tip with a spot size of approximately 20 µm. We used a self-homodyne detection scheme[18,57], which yielded stable detection of the scattered signal and good signal contrast. A schematic of the m-SNOM and cryostat is shown in Extended Data Fig. 1.

Device fabrication

All samples used in this work were hBN-encapsulated monolayer graphene field-effect devices, fabricated through the standard dry-transfer[58] and nanolithography techniques. The top and bottom hBN and monolayer graphene crystals were first mechanically exfoliated onto SiO$_2$(285 nm)/Si substrates. A polydimethylsiloxane/polycarbonate (PC) stamp was then used to pick up the top hBN at ~120 °C, followed by graphene at ~100 °C and finally the bottom hBN at ~120 °C. The assembled hBN–graphene–hBN stack was then released onto a clean SiO$_2$(285 nm)/Si substrate by melting the PC at ~180 °C. After removing the bulk part of the PC in chloroform, the transferred stack was annealed in forming gas (5% H$_2$/95% Ar) at 350 °C for 2 h to further remove the PC residue. Standard electron beam lithography was used to define the source and drain electrodes using an A4 950PMMA resist. The exposed pattern was developed in a water/isopropyl alcohol (1:3) solution at a temperature of 5 °C for 2 min. The top hBN and graphene at the contact area were then etched in CHF$_3$/O$_2$ (10:1) plasma (40 mTorr and 60 W), exposing the side of the graphene layer. Cr(5 nm)/Au(40 nm) was then thermally evaporated to form side contacts for the graphene[59].

Reporting summary

Further information on the research design is available in the Nature Portfolio Reporting Summary linked to this article.

Data availability

The data represented in Figs. 1–4 are available as Source Data 1–4. All other data that support the findings of this study are available from the corresponding authors upon reasonable request.

Code availability

All codes underlying this study are available from the corresponding authors upon reasonable request.

References

57. Knoll, B. & Keilmann, F. Enhanced dielectric contrast in scattering-type scanning near-field optical microscopy. *Opt. Commun.* **182**, 321–328 (2000).
58. Purdie, D. G. et al. Cleaning interfaces in layered materials heterostructures. *Nat. Commun.* **9**, 5387 (2018).
59. Wang, L. et al. One-dimensional electrical contact to a two-dimensional material. *Science* **342**, 614–617 (2013).

Author contributions

M.D., M.T., X.C., L.W., W.Z., D.N.B. and M.K.L. designed the experiment. M.D., M.T., L.W., S.Z., X.D. and M.K.L. performed the measurements. X.D. and J.S. fabricated the samples. M.D., M.T., Z.D., X.C., L.W., W.Z. S.X., Y.D., V.R., M.P., Z.Z., A.B., G.L.C., Q.L., A.B.K., A.G., X.D., M.M.F. and M.K.L. analysed the data. M.T., X.C., W.Z., S.X., Y.S., R.J. and D.H. performed the simulations. M.D. and M.K.L wrote the paper. All authors contributed to the scientific discussions and paper revisions.

Competing interests

M.D., X.C., M.K.L. and A.G. have a patent pending related to the design of the m-SNOM. The other authors declare no competing interests.

Additional information

Extended data Extended data are available for this paper at https://doi.org/10.1038/s41565-023-01488-y.

Supplementary information The online version contains supplementary material available at https://doi.org/10.1038/s41565-023-01488-y.

Correspondence and requests for materials should be addressed to D. N. Basov, Xu Du or Mengkun Liu.

Peer review information *Nature Nanotechnology* thanks the anonymous reviewers for their contribution to the peer review of this work.

Reprints and permissions information is available at www.nature.com/reprints.
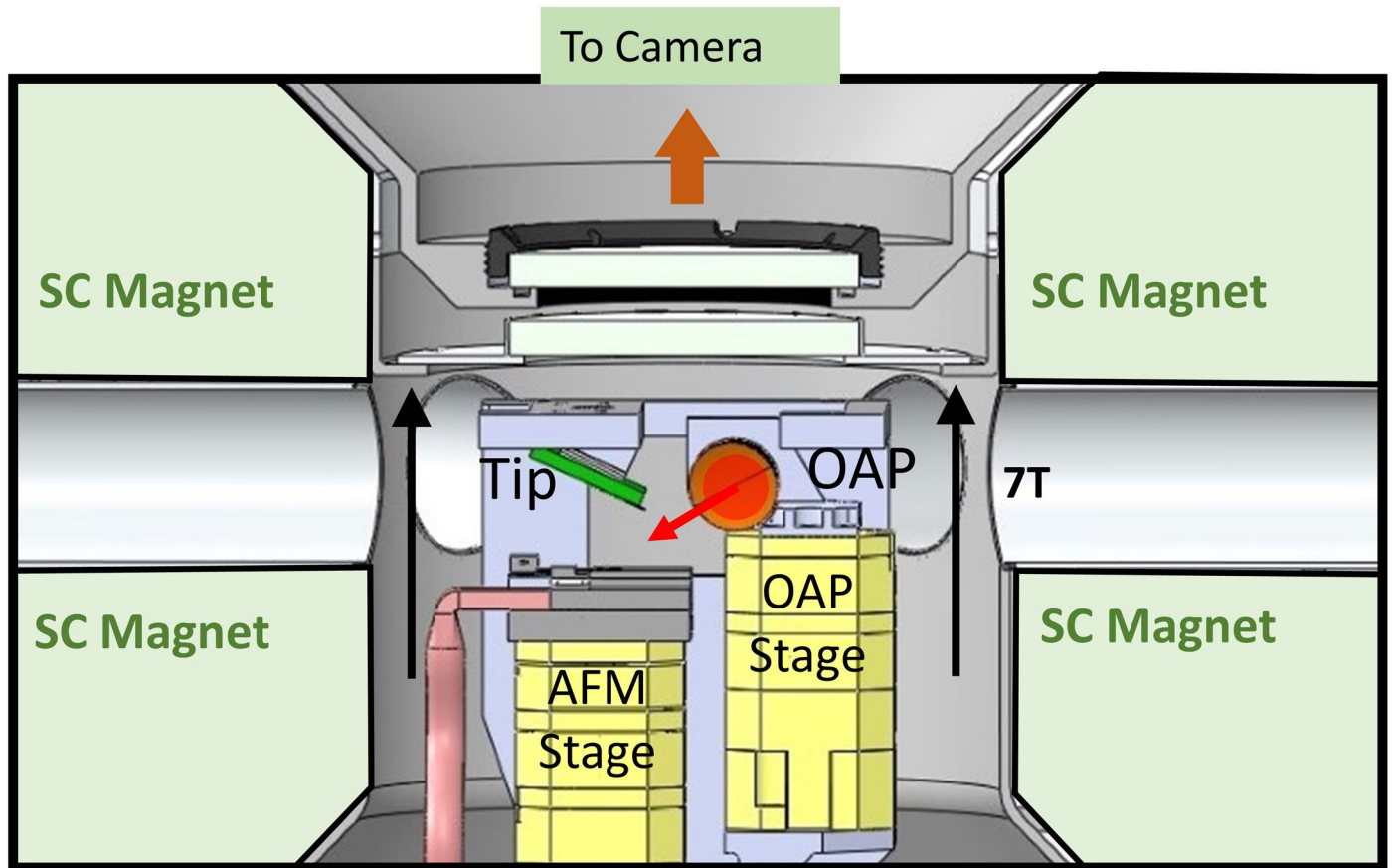
Extended Data Fig. 1 | Closed-cycle m-SNOM setup. OAP: off-axis parabolic mirror. Tip: Akiyama probe. Light enters the chamber in the horizontal direction (into the field of view) and is focused onto the sample with an OAP.

nature research

Corresponding author(s):   Michael Dapolito

☐ Initial submission   ☐ Revised version   ☒ Final submission

Lasing Reporting Summary

Nature Research wishes to improve the reproducibility of the work that we publish. This form is intended for publication with all accepted papers reporting claims of lasing and provides structure for consistency and transparency in reporting. Some list items might not apply to an individual manuscript, but all fields must be completed for clarity.

For further information on Nature Research policies, including our data availability policy, see Authors & Referees.

Experimental design

Please check: are the following details reported in the manuscript?

1. Threshold

   Plots of device output power versus pump power over a wide range of values indicating a clear threshold

   ☐ Yes | *State where this information can be found in the text.*
   ☒ No | Not relevant to the experiment.

2. Linewidth narrowing

   Plots of spectral power density for the emission at pump powers below, around, and above the lasing threshold, indicating a clear linewidth narrowing at threshold

   ☐ Yes | *State where this information can be found in the text.*
   ☒ No | Not relevant to the experiment.

   Resolution of the spectrometer used to make spectral measurements

   ☐ Yes | *State where this information can be found in the text.*
   ☒ No | Precise replication of the laser power used is not needed to reproduce experiment.

3. Coherent emission

   Measurements of the coherence and/or polarization of the emission

   ☐ Yes | *State where this information can be found in the text.*
   ☒ No | Can be obtained from Access Laser.

4. Beam spatial profile

   Image and/or measurement of the spatial shape and profile of the emission, showing a well-defined beam above threshold

   ☐ Yes | *State where this information can be found in the text.*
   ☒ No | Not necessary to reproduce experiment.

5. Operating conditions

   Description of the laser and pumping conditions
   Continuous-wave, pulsed, temperature of operation

   ☒ Yes | Methods section
   ☐ No | *Explain why this information is not reported/not relevant.*

   Threshold values provided as density values (e.g. W cm^{-2} or J cm^{-2}) taking into account the area of the device

   ☐ Yes | *State where this information can be found in the text.*
   ☒ No | Not necessary to reproduce experiment.

6. Alternative explanations

   Reasoning as to why alternative explanations have been ruled out as responsible for the emission characteristics
   e.g. amplified spontaneous, directional scattering; modification of fluorescence spectrum by the cavity

   ☐ Yes | *State where this information can be found in the text.*
   ☒ No | Not relevant to the experiment.

7. Theoretical analysis

   Theoretical analysis that ensures that the experimental values measured are realistic and reasonable
   e.g. laser threshold, linewidth, cavity gain-loss, efficiency

   ☐ Yes | *State where this information can be found in the text.*
   ☒ No | Not relevant to the experiment.

8. Statistics

   Number of devices fabricated and tested

   ☐ Yes | *State where this information can be found in the text.*
   ☒ No | Not relevant to the experiment.

   Statistical analysis of the device performance and lifetime (time to failure)

   ☐ Yes | *State where this information can be found in the text.*
   ☒ No | Can be obtained from Access Laser.

Further reading

We also suggest that authors read the following literature, which describes the important principles and signatures of laser emission and discusses some of the common mistakes that can occur during laser characterization.

1. Samuel I.D.W., Namdas, E.B. & Turnbull, G.A. How to recognize lasing. *Nat. Photon.* **3**, 546-549 (2009).
2. Siegmann, A.E. *Lasers*. (University Science Books, 1990)
3. Svelto, O. *Principles of Lasers*. 5th edn. (Springer 2010)
4. Blood, P. *Quantum Confined Laser Devices: Optical Gain and Recombination in Semiconductors*. (Oxford Univ. Press, 2015)
5. Koxlov, V.G. *et al*. Laser action in organic semiconductor waveguide and double-heterostructure devices. *Nature* **389**, 362-364 (1997).

Infrared nano-imaging of Dirac magnetoexcitons in graphene

In the format provided by the
authors and unedited

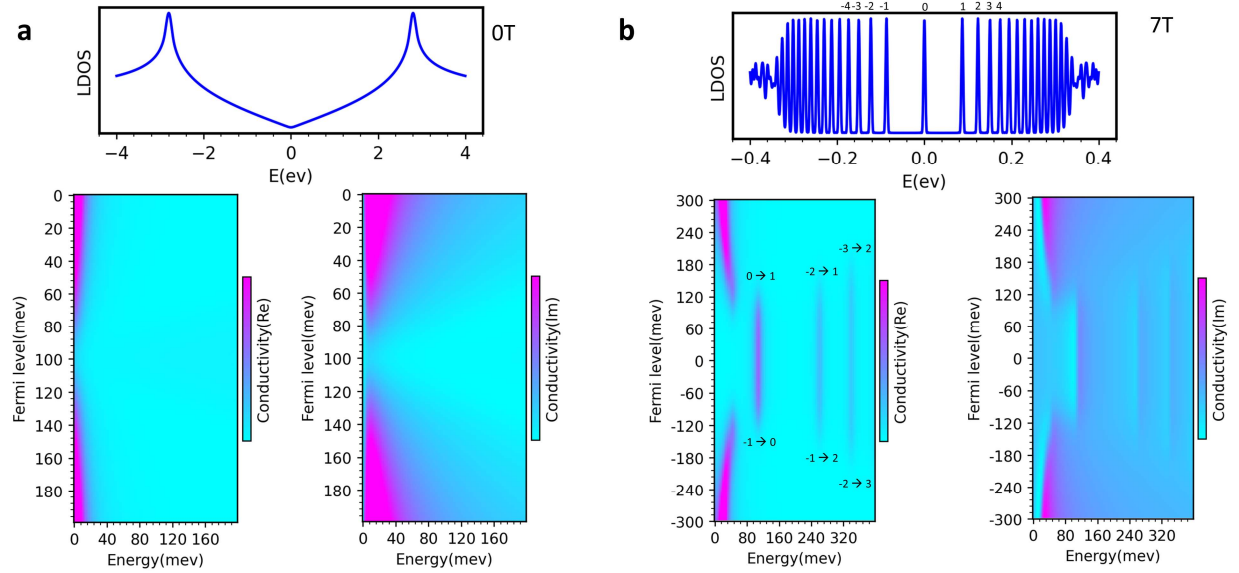# S1. Magneto-Optical Conductivity Calculation

Fig.S1. *Local density of states (LDOS) of electrons (top) and 2D maps of the optical conductivity (bottom) of charge-neutral graphene at magnetic fields at 0 T (**a**) and 7 T (**b**).*
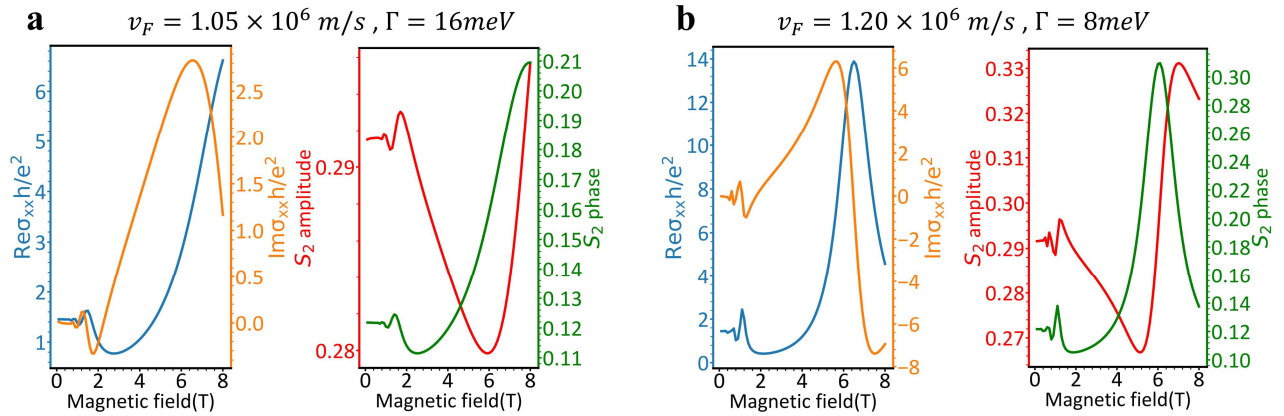

Fig.S2. Magneto-optical conductivity (σ_{xx}) and near-field scattering signal (S_2) calculations at two different parameter sets, indicated at the top of a and b. v_F *is the Fermi velocity and Γ is the scattering rate. The S_2 amplitude at 7 T is higher for the higher v_F (the peak shifts to a lower magnetic field). The scattering rate determines the width of the peaks in σ_{xx} and S_2.*
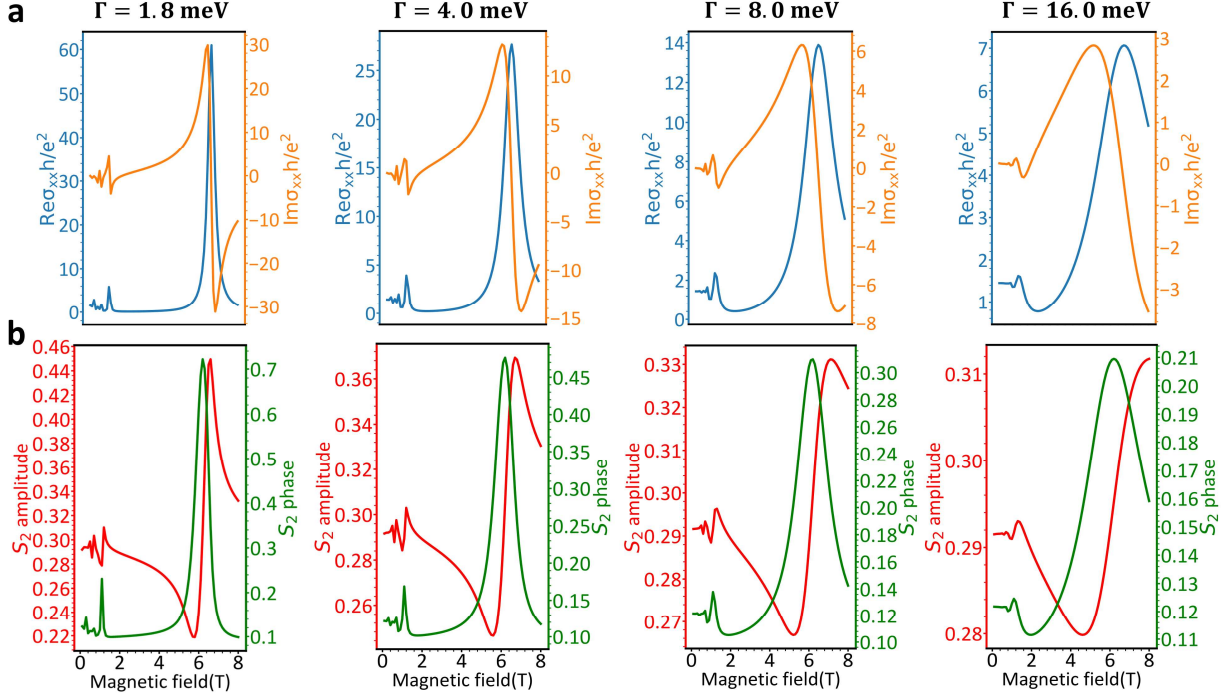
Fig.S3. *Magneto-optical conductivity, σ_{xx} (a) and near-field scattering signal S_2 (b) as the phenomenological scattering rate Γ is varied. As the scattering rate increases, the broadening of the LL transition is shown as a broadening in both the conductivity and SNOM scattering signal. We found that our calculations and simulations best match the experimental data when carried out at $\Gamma = 8\ meV$. Parameters: $v_F = 1.19 \times 10^6\ m/s$ and $T = 200\ K$.*

The infrared magneto-optical conductivity in graphene is calculated based on Kubo formula and an energy-independent scattering rate approximation [4]. Similar approaches are used and agree well with the experimental results in both the terahertz and infrared frequency ranges [32,60,61].

The longitudinal conductivity of graphene in a magnetic field can be analytically expressed as

$$\sigma_{xx}(\omega) = i\frac{e^2}{2\pi}(\hbar\omega_c)^2$$
$$\times \sum_{n=0}^{\infty} \sum_{s=\pm 1} \frac{\omega + i\Gamma}{E_{sn} - E_{n+1}} \frac{f(E_{sn}) - f(E_{n+1}) + f(E_{-(n+1)}) - f(E_{-sn})}{(E_{sn} - E_{n+1})^2 - (\omega + i\Gamma)^2} \quad \text{(S1)}$$

where Γ is the scattering rate, which determines the broadening of LL transitions and is assumed to be independent of frequency and LL index, $f(E_n) = \frac{1}{e^{(E_n - \mu)/k_B T} + 1}$ is the Fermi-Dirac distribution function, and $E_n = \text{sgn}(n)\sqrt{2|n|v_F^2|eB|/c}$ is the LL energy. The accuracy of the calculated magneto-optical conductivity is determined by the number of inter-Landau level

transitions and a smaller magnetic field would require more LLs included in the calculation. A total of 80,000 LLs are included in the calculation and the formula reproduces the graphene conductivity in the low field limit in the energy range we considered in this work. The calculated conductivities are used to compute the reflection coefficients r_p of the heterostructure, that is, hBN-graphene-hBN on SiO_2/Si substrate. The resultant coefficients are used in near-field calculations based on the Lightning Rod model [62]. The calculated σ_{xx} and S_2 are plotted in Figs. S2 and S3. The reflection coefficient r_p has the following form in the near-field limit:

$$r_p(q,\omega) = 1 - \frac{\varepsilon_0}{\kappa - \frac{2\pi\sigma_{xx}}{i\omega}|q|} , \qquad q \gg \frac{\omega}{c} . \qquad (S2)$$

Here ε_0 is the permittivity of vacuum, $\kappa = \varepsilon_0/(1 - r_p^*) = \kappa_1 + i\kappa_2$ is the effective permittivity of the graphene environment, and r_p^* is the reflection coefficient that the system would have in the absence of graphene. The poles of $r_p(q,\omega)$ analytically continued to complex momenta $q = q_1 + iq_2$ define the DiME dispersion. Such poles exist at $q = i\omega\kappa/2\pi\sigma_{xx}$ if $\sigma_2 > 0$ [15,32,63]. The magnetic field dependent $r_p(q)$ at $\omega = 900\ cm^{-1}$ is plotted in Fig. S4.
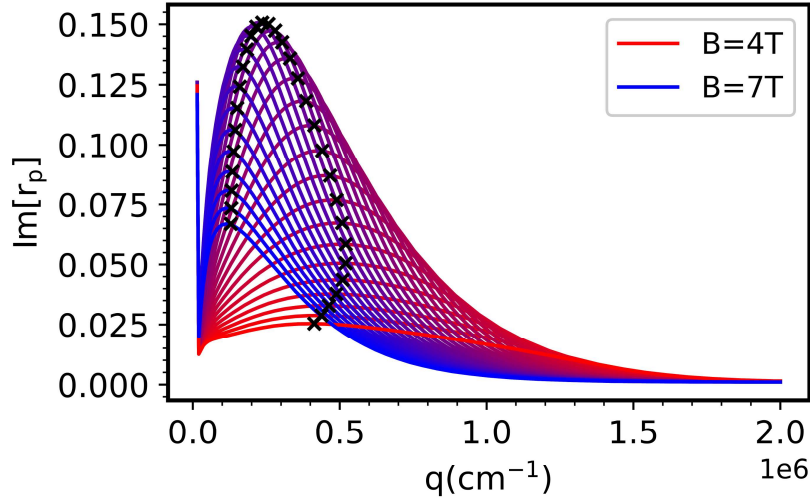

Fig.S4. The calculated magnetic field-dependent reflection coefficient r_p from 4 T (red) to 7 T (blue). *The peak position of r_p indicates approximately the plasmon wave vector $q_p = 2\pi/\lambda_p$. The width of the r_p indicates the Q factor of the DiME. With a typical Fermi velocity $v_F = 1.19 \times 10^6$ m/s and a scattering rate $\Gamma = 8\ meV$, the Q factor of the DiME is approximately 3 at ~110 meV, 7 T, and 200 K.*

S1.1. DiME Quality Factor

As the contribution to the Q factor from phonon scattering is much smaller compared to the contribution from the impurity scattering rate[64] at our temperature range, the Q factor can be improved by decreasing the impurity scattering rate (Fig. S5). This can be achieved by increasing the sample quality and reducing the temperature[65]. For high quality samples at low temperatures (e.g. below 10 K), the DiME Q factor can in principle be increased to above 10, as shown in Fig. S5.
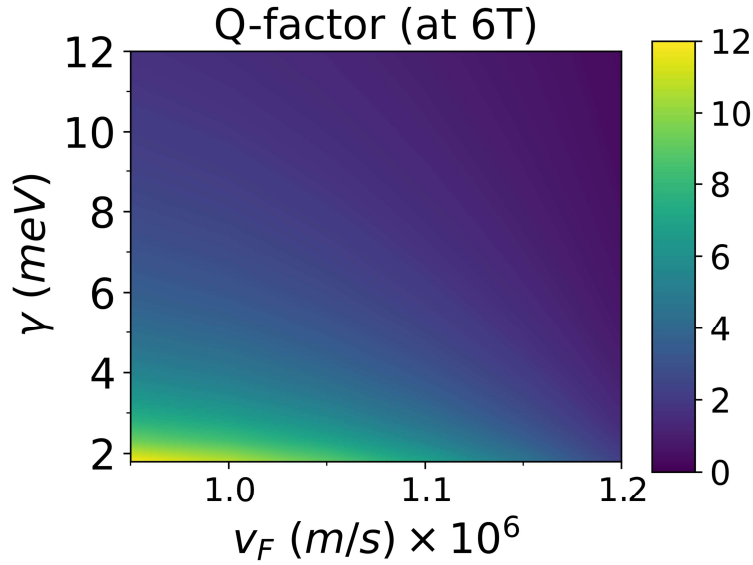

Fig.S5. *Quality factor of the DiME as a function of impurity scattering rate and Fermi velocity. The factor Q is calculated as the ratio of $Im(\sigma_{xx})/Re(\sigma_{xx})$ using the magneto-optical conductivity calculations described in this section. A maximum Q factor of 12 can be achieved for samples of sufficiently high quality.*

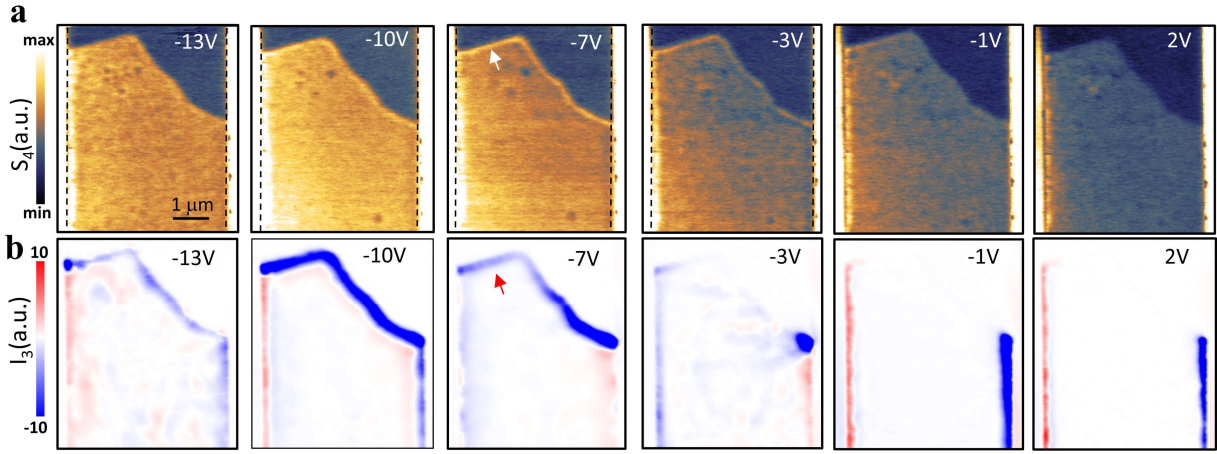## S2. Gate dependence of the s-SNOM and photocurrent signals.

Fig.S6. *Gate-dependent near-field scattering S$_4$ (**a**) and near-field photocurrent I$_3$ (**b**), images of the graphene edge at -6.6 T. The CNP is at around -9.5 V.*

In Fig. S6 the back-gate-dependent s-SNOM (S$_4$) and photocurrent (I$_3$) images show that when the Fermi level is increased to close to and beyond the 1st Landau level the edge DiME polariton fringe (indicated by the white arrow) and edge photocurrent (indicated by the red arrow) disappear correspondingly. Fig. S6 illustrates the importance of near-charge neutrality in this study.

S3. Simulation of near-field photocurrent measurements

The simulation of near-field photocurrent imaging follows the Shockley-Ramo (SR) formalism [66] that has been successfully utilized to describe real-space photocurrent data in conventional far-field measurements [40,67] and near-field nano-photocurrent studies [30,31,68]. There are two kinds of current in graphene, the local photocurrent generated under the tip owing to the thermoelectric effect as $\boldsymbol{j}_{loc}(\boldsymbol{r}) = \boldsymbol{\alpha} \cdot \nabla T$, and the diffusion current due to ambient carriers driven by electrochemical potential ϕ as $\boldsymbol{j}_d = -\boldsymbol{\sigma} \cdot \nabla \phi$, where $\boldsymbol{\alpha} = \begin{bmatrix} \alpha_{xx} & \alpha_{xy} \\ -\alpha_{xy} & \alpha_{xx} \end{bmatrix}$ and $\boldsymbol{\sigma} = \begin{bmatrix} \sigma_{xx} & \sigma_{xy} \\ -\sigma_{xy} & \sigma_{xx} \end{bmatrix}$ are the dc thermoelectric conductivity matrix and dc conductivity matrix, respectively [40,66]. The total currents obey the continuity equation, so $\nabla \cdot (\boldsymbol{j}_d + \boldsymbol{j}_{loc}) = 0$.

In the SR formalism, we define the auxiliary weighting field ψ and its accompanying auxiliary current $\boldsymbol{j}_\psi = -\boldsymbol{\sigma}^T \nabla \psi$ on the graphene domain. It satisfies the Laplace equation as $\nabla \cdot \boldsymbol{j}_\psi = 0$ with the natural boundary conditions: $\boldsymbol{n} \cdot \boldsymbol{j}_\psi = 0$ at the sample-vacuum interface (non-contact edge), and $\boldsymbol{n} \times \nabla \psi = 0$ at the sample-contact interface (contact edge), where $\boldsymbol{n}$ is the unit vector normal to the boundary. In our calculation, for simplicity, ψ is set to 1 at the current-collecting contacts

and 0 at the grounded contacts. The measured photocurrent I_{PC} is now related to the local photocurrent $\boldsymbol{j}_{loc}$ as:

$$I_{PC} = \iint \nabla\psi(\boldsymbol{r}') \cdot \boldsymbol{j}_{loc}(\boldsymbol{r}')d^2\boldsymbol{r}' \tag{S3}$$

Near the edge,

$$
\begin{aligned}
I_{PC} &= \iint \nabla\psi(\boldsymbol{r}') \cdot \boldsymbol{\alpha}\nabla T(\boldsymbol{r}')d^2\boldsymbol{r}' \\
&= \alpha_{xx}\iint \nabla \cdot (T\nabla\psi)d^2\boldsymbol{r}' + \alpha_{xy}\iint \nabla \times (T\nabla\psi)d^2\boldsymbol{r}' \\
&= \alpha_{xx}\int T\nabla\psi \cdot d\boldsymbol{n} + \alpha_{xy}T|\nabla\psi \times d\boldsymbol{n}|
\end{aligned}
$$

Where $\boldsymbol{n}$ is the normal vector of the boundary. At the contact edge, where $\boldsymbol{n} \times \nabla\psi = 0$, the second term is eliminated. At the non-contact edge, where $\boldsymbol{n} \cdot (\boldsymbol{\sigma}^T\nabla\psi) = 0$, $\frac{\nabla_\perp\psi'}{\nabla_\parallel\psi'} = \frac{\sigma_{xy}}{\sigma_{xx}}$. Therefore:

$$
I_{PC} = \begin{cases}
\alpha_{xx}\int T\nabla\psi \cdot d\boldsymbol{n}, & at\ the\ contact\ edge \\
\pm\dfrac{\alpha_{xx}\sigma_{xy} - \alpha_{xy}\sigma_{xx}}{\sqrt{\sigma_{xx}^2 + \sigma_{xy}^2}}\int T|\nabla\psi'|dl, & at\ the\ non-contact\ edge
\end{cases}
$$

Besides, $\boldsymbol{\sigma}$ and $\boldsymbol{\alpha}$ of graphene obey the following equation:

$$\boldsymbol{\sigma}(B) = -\int_{-\infty}^{\infty} \boldsymbol{\sigma_0}(\varepsilon, B)\frac{\partial f}{\partial \varepsilon}d\varepsilon$$

$$\boldsymbol{\alpha}(B) = \frac{1}{e}\int_{-\infty}^{\infty} \boldsymbol{\sigma_0}(\varepsilon, B)\frac{\partial f}{\partial T}d\varepsilon$$

Where f is Fermi-Dirac distribution, $\boldsymbol{\sigma_0}(\varepsilon, B)$ is the electrical conductivity tensor of the charge carriers at energy ε on the external perpendicular magnetic field, which can be calculated with Eqs. (3.11- 3.15) from [69].

We calculate $\boldsymbol{\alpha}$ and $\boldsymbol{\sigma}$ as the magnetic field is swept from -7 T to 7 T at 200 K using a scattering rate of 8 meV, a Fermi velocity of 1.19×10^6 m/s, a chemical potential of 20 meV, as graphene is close to the charge-neutral point but possibly still with a small offset. The dependence of diagonal and off-diagonal components of $\boldsymbol{\alpha}$ and $\boldsymbol{\sigma}$ on the magnetic field is plotted in Fig. S7.
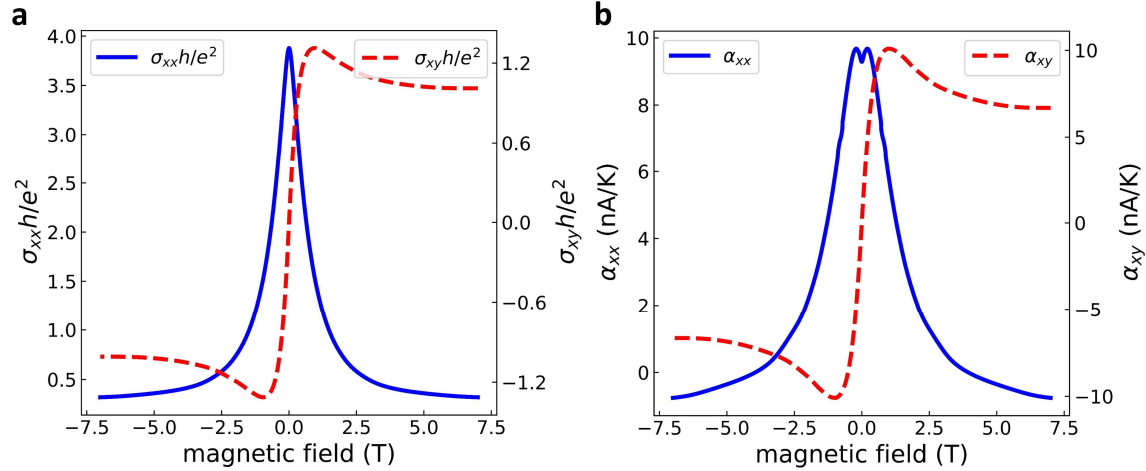
Fig.S7. Calculated electrical and thermoelectrical conductivity for T = 200 K, impurity scattering rate = 8 meV, Fermi velocity = 1.19×10^6 m/s, and gap energy = 0 meV. a, *The calculated field-dependent diagonal (σ_{xx}, blue curve, left axis) and off-diagonal (σ_{xy}, red curve, right axis) electrical conductivity of graphene.* ***b,*** *The calculated field-dependent diagonal (α_{xx}, blue curve, left axis) and off-diagonal (α_{xy}, red curve, right axis) thermoelectrical conductivity of graphene.*
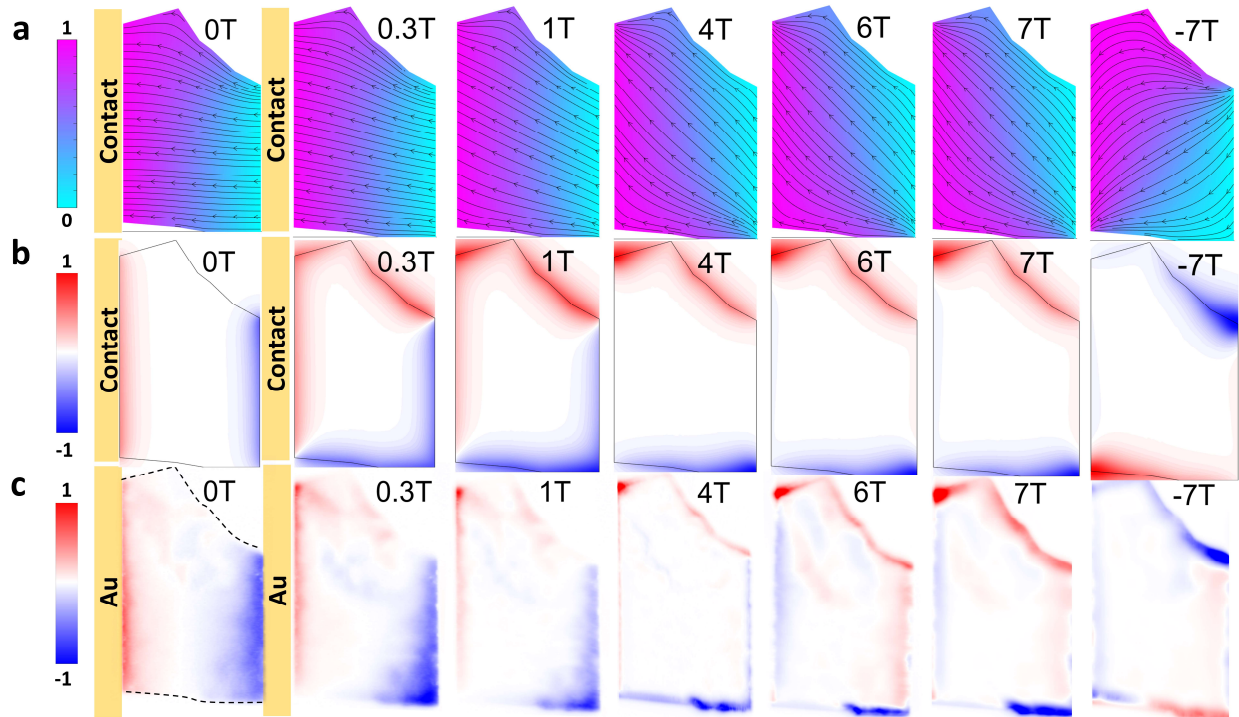

Fig.S8. Comparison between simulated and experimental photocurrent mappings. a, *calculated field-dependent auxiliary weighting field ψ (colormap) and auxiliary current j$_\psi$ (streamlines).* ***b,c,***

*Simulated (**b**) and experimental (**c**) (from Fig. 2b) photocurrent I_{PC} map. The gold contacts are only shown in the first panel in each column.*

Using the calculated $\boldsymbol{\alpha}(B)$ and $\boldsymbol{\sigma}(B)$, we calculated the auxiliary weighting field ψ (Fig. S8a colormap), auxiliary current $\boldsymbol{j}_\psi$ (Fig. S8a streamlines) and photocurrent (Fig. S8b) for the two-terminal graphene device as seen in the experiment, whose left and right edges contact the gold electrodes, and the top and bottom edges are free of contacts.

In zero magnetic field, where $\sigma_{xy} = 0$ and $\alpha_{xy} = 0$ (see Fig. S7), $\boldsymbol{j}_\psi$ is parallel to the non-contact graphene edge and the photocurrent near the free boundary vanishes according to Eq. 2. As the magnetic field increases, α_{xx} decreases and σ_{xy} becomes nonzero (see Fig. S7), hence the contacted edge photocurrent fades out while the non-contact edge photocurrent emerges. With increasing fields, the streamlines of $\boldsymbol{j}_\psi$ start to orient diagonally across the graphene sheet, so that the photocurrent is locally enhanced at two opposite corners. As B sweeps from ± 4 T to ± 7 T, the photocurrent pattern close to the non-contacted edge has no significant change because of the slowly varying σ_{xy} and α_{xy}. In addition, σ_{xy} switches sign with opposite magnetic fields. Correspondingly, the photocurrent hot spots move to the other pair of corners.

We attribute the disagreement between the calculation and experiment at the bottom-left corner to the defects in graphene. We note that the simulated photocurrent near the non-contacted edge is not as strong as the one in experiments at ± 7 T since we do not include Landau transition-enhanced light absorption in the simulation.

Supplementary Information References

60.   Li, Z. Q. *et al.* Infrared probe of the anomalous magnetotransport of highly oriented pyrolytic graphite in the extreme quantum limit. *Phys Rev B* **74**, 195404 (2006).

61.   Yumoto, G., Matsunaga, R., Hibino, H. & Shimano, R. Ultrafast Terahertz Nonlinear Optics of Landau Level Transitions in a Monolayer Graphene. *Phys Rev Lett* **120**, 107401 (2018).

62.   Bouhelier, A. Field-enhanced scanning near-field optical microscopy. *Microscopy Research and Technique* vol. 69 563–579 Preprint at https://doi.org/10.1002/jemt.20328 (2006).

63.   Walsh, B. M., Foster, J. C., Erickson, P. J. & Sibeck, D. G. Tunable Phonon Polaritons in Atomically Thin van der Waals Crystals of Boron Nitride. *Science (1979)* **343**, 1122–1125 (2014).

64.   Funk, H., Knorr, A., Wendler, F. & Malic, E. Microscopic view on Landau level broadening mechanisms in graphene. *Phys Rev B Condens Matter Mater Phys* **92**, 205428 (2015).

65.   Sarkar, S. *et al.* Role of different scattering mechanisms on the temperature dependence of transport in graphene. *Scientific Reports 2015 5:1* **5**, 1–10 (2015).

66. Song, J. C. W. & Levitov, L. S. Shockley-Ramo theorem and long-range photocurrent response in gapless materials. *Phys Rev B* **90**, 75415 (2014).

67. Ma, Q. *et al.* Giant intrinsic photoresponse in pristine graphene. *Nature Nanotechnology* vol. 14 145–150 Preprint at https://doi.org/10.1038/s41565-018-0323-8 (2019).

68. Hesp, N. C. H. *et al.* Nano-imaging photoresponse in a moiré unit cell of minimally twisted bilayer graphene. *Nat Commun* **12**, (2021).

69. Gusynin, V. P. & Sharapov, S. G. Transport of Dirac quasiparticles in graphene: Hall and optical conductivities. (2006) doi:10.1103/PhysRevB.73.245411.